Journal of Environmental Chemical Engineering 13 (2025) 118854

Contents lists available at ScienceDirect

Journal of Environmental Chemical Engineering

journal homepage: www.elsevier.com/locate/jece

Stable Ni-decorated $CaTiO_3/WO_3/BiVO_4$ multi-layered photoanodes for improved solar-driven water oxidation at high current densities

Sara Crespo [a,*], Ivan Merino-Garcia [a], Maite Perfecto-Irigaray [b,c], Garikoitz Beobide [b,d], Jonathan Albo [a,*]

[a] Departamento de Ingenierías Química y Biomolecular, Universidad de Cantabria, Avenida de los Castros s/n, Santander 39005, Spain
[b] Department of Organic and Inorganic Chemistry, University of the Basque Country, UPV/EHU, P.O. 644, Bilbao 48080, Spain
[c] ISIS Neutron and Muon Source, STFC Rutherford Appleton Laboratory, Didcot OX110QX, UK
[d] BCMaterials, Basque Center for Materials, Applications and Nanostructures, UPV/EHU Science Park, Leioa 48940, Spain

ARTICLE INFO

Keywords:
Photoelectrocatalysis
Oxygen evolution reaction
Ni-based photoanodes
Visible light

ABSTRACT

Conventional electrochemical systems involving the oxygen evolution reaction (OER) in the anodic compartment suffer from low efficiency and high energy consumption, accounting for over 90 % of the total energy input, thereby hindering the practical application of this technology. The reliance on external energy can be decreased by coupling external renewable energy sources, such as solar energy, through a sustainable photoelectrochemical (PEC) approach driven by efficient photoanodes. In this study, we present the automated fabrication and optimization of multi-layered Ni-decorated $CaTiO_3/WO_3/BiVO_4$ photoanodes, supported onto FTO substrates, for enhanced PEC water oxidation under visible-light illumination. Different photoanode configurations are fabricated via layer-by-layer deposition, with the top layer consisting of either sequentially deposited Ni and $BiVO_4$ layers or a physical mixture of the two materials. The mixed Ni-$BiVO_4$ top layer configuration strengthens the synergistic interaction between components, resulting in enhanced PEC performance with a cathodic potential as low as −1.17 V vs. Ag/AgCl at a practically relevant current density of 100 mA cm^{-2}. Furthermore, the applied bias photon-to-current efficiency (ABPE) for this optimized photoanode configuration reaches a maximum of 0.52 %, corresponding to an O_2 production rate of 2 μmol cm^{-2} h^{-1} under visible light (100 mW cm^{-2}). Overall, this work demonstrates how optimizing multi-layered photoanodes enables operation at current densities relevant for practical applications, paving the way for their integration in PEC systems.

1. Introduction

The global energy landscape is changing rapidly, as efforts to address climate change and improve energy security gain significant momentum, driving a transition to cleaner and more sustainable energy solutions [1]. Among the methods for energy production and storage, conventional electrochemical (EC) systems have been widely studied and used for their ability to drive redox reactions such as the hydrogen evolution reaction (HER) and CO_2 reduction reaction (CO_2RR) [2]. These systems rely entirely on external energy sources to activate the necessary reactions at the electrodes. However, despite their technological maturity and scalability, this process still faces significant challenges that hinder its development and practical application [3]. These include the high energy consumption, mainly due to the oxygen evolution reaction (OER), which accounts for more than 90 % of the total energy input (130 kWh per kilogram) [3,4], the high overall cost, and the limited durability of the cathode, among other issues [5]. Part of the external energy demand can be met by coupling the electrochemical system with external renewable energy sources, such as solar energy, in a sustainable photoelectrochemical (PEC) approach driven by photoresponsive anodes [6]. In this way, solar energy is harnessed in a photoactive surface to provide an extra flow of electrons (e^-) toward the cathode, thus improving the reduction of CO_2 to value-added products or the production of green H_2 through PEC water splitting in the cathode, as well as facilitating the OER [7,8]. PEC strategies can drastically lower the energy and carbon footprint of electrochemical processes [9,10]. Recent studies have further explored advanced configurations, such as coupling anodic glycerol electrooxidation with H_2 generation, to improve the overall efficiency of PEC systems [9,10]. The development of efficient PEC systems, however, remains limited by the performance

* Corresponding authors.
E-mail addresses: sara.crespo@unican.es (S. Crespo), jonathan.albo@unican.es (J. Albo).

https://doi.org/10.1016/j.jece.2025.118854
Received 20 June 2025; Received in revised form 8 August 2025; Accepted 20 August 2025
Available online 21 August 2025

of photoactive catalysts and the need for materials capable of operating at high current densities with significant stability and durability [11, 12].

The heterostructure/multi-layered construction is one of the most promising strategies to improve the performance of PEC processes and enhance the photostability of materials used as photoanodes [13–15]. Semiconductors such as $BiVO_4$, TiO_2, ZnO, FeOOH, and Fe_2O_3 are commonly used for PEC water oxidation due to their ability to improve light absorption, facilitate more effective separation of photogenerated charge carriers, and enhance the stability of the photoelectrode [16].

Nevertheless, some of these semiconductors have limited solar energy harvesting capabilities due to their wide bandgaps, high charge recombination rates, and stability limitations in aqueous environments, which ultimately reduce the efficiency of solar-driven PEC processes [17,18].

Bismuth(III) vanadate ($BiVO_4$) has attracted considerable attention due to its suitable bandgap (~2.4 eV), which allows it to absorb visible light, low cost, and the high photovoltage (>1 V) generated at the semiconductor-liquid junction [19]. The main challenges that still make the practical application of $BiVO_4$ difficult are its low electrical conductivity and slow surface reaction kinetics for water oxidation [20]. Moreover, tungsten oxide (WO_3) represents an earth-abundant visible--light n-type semiconductor noted for its remarkable chemical stability and electrical conductivity. WO_3 presents a bandgap ranging from 2.5 to 2.8 eV, providing absorption of approximately 12 % of the solar spectrum [21]. Previous work in our group included the automated and reproducible fabrication of multi-layered $BiVO_4/WO_3$ photoanodes with different mass ratios supported onto porous Toray carbon paper for PEC under front-illumination conditions [22]. The physicochemical characterization showed that the highest photoactivity is reached with the photoanode $BiVO_4/WO_3$ (80:20), associated with an improved visible light absorption ($BiVO_4$ as the top layer) due to the narrow bandgap of the monoclinic $BiVO_4$ structure and synergetic effects between $BiVO_4$ and WO_3, leading to higher current densities at the cathode. The optimized $BiVO_4/WO_3$ photoanode achieved a photocurrent of -2.3 mA cm^{-2}, leading to a significant 15 % increase compared to a bare $BiVO_4$ photoelectrode (-2 mA cm^{-2}) at −2 V vs. Ag/AgCl under an illumination intensity of 100 mW cm^{-2} (1 sun) [22]. As bare $BiVO_4$ suffers from poor electron conductivity and slow OER kinetics [23], the addition of WO_3 may help improve efficiency by facilitating electron transfer from $BiVO_4$ and reducing charge transfer resistance [24,25]. On the other hand, titanate-based perovskites are excellent semiconducting materials for solar energy conversion applications due to their unique electronic and structural properties, high stability, and corrosion resistance in aqueous solutions [26]. In particular, calcium titanate ($CaTiO_3$) presents a relatively wide bandgap of approximately 3.4 eV. Although the absorption of visible light can be limited, $CaTiO_3$ can serve as an excellent electron collector in a multi-layered structure, thus enhancing charges separation [27]. Previous work on optimizing the configuration of a multi-layered $CaTiO_3$ (bottom layer) photoelectrode with $BiVO_4$ (top layer) revealed that back illumination with Fluoride-doped Tin Oxide (FTO) supports leads to an improved PEC process performance when adjusting the $CaTiO_3/BiVO_4$ mass ratio in comparison with the performance of the photoelectrodes under front-illumination conditions [28].

Recent studies have also demonstrated that metallic surface modifications, especially those containing Fe, Cr, or Ni, can form catalytically active NiFe(oxy)hydroxide species that boost OER activity while protecting the underlying semiconductor from degradation [29]. Particularly, Ni has demonstrated its potential to effectively reduce the bandgap of the heterostructure, increase the specific surface area and broaden the light absorption spectrum [30,31]. Indeed, Ni doping has been shown to enhance the photocurrent density of $BiVO_4$-based photoanodes by a factor of three in comparison with undoped samples, which is attributed not only to enhanced OER catalysis, but also improved charges separation process [23,32].

Taking all this into consideration, the present work focuses on the design, development, and optimization of advanced Ni-decorated multi-layered $BiVO_4/WO_3/CaTiO_3$ photoanodes for the OER, which are then integrated into a PEC electrolyzer operating under continuous single-pass conditions at relevant current densities. The study provides novel insights into photoanodes optimization, proposing strategies to enhance light harvesting and OER performance. By addressing key challenges such as charge separation, light absorption, and limited current densities, this work advances the development of energy-efficient PEC production systems in continuous operation, bridging the gap between laboratory-scale research and practical solar-driven applications.

2. Materials and methods

2.1. Photoanodes preparation

The materials used in this study to fabricate the multi-layered photoanodes include commercial $CaTiO_3$ nanopowder (< 100 nm, 99 %, Aldrich Chemistry), WO_3 nanopowder (< 100 nm, 99,995 %, Aldrich Chemistry), $BiVO_4$ mesh powder (~200 μm, 99,9 %, Alfa Aesar) and Ni nanopowder (< 100 nm, 99 %, Aldrich Chemistry). The inks consist of isopropanol (laboratory reagent grade, ≥99.5 %, Fisher Chemicals) as the solvent (97 wt%) and a Nafion D521 binder (5 wt% dispersion, Ion Power), with a catalyst/binder ratio of 70/30 [33]. The ink solutions are prepared and sonicated for 1 h to ensure homogeneity and proper dispersion of the materials.

The automated and reproducible fabrication process involves a systematic deposition of distinct layers onto a transparent FTO support (FTO-coated glass substrate 2.2 mm, 12–15 Ω sq^{-1}, MSE supplies). The photoanodes are manufactured with a geometric area of 10 cm^2 using a spray pyrolysis technique (ND-DP Mini Ultrasonic Spray Coater, Nadetech Innovations), as presented in Fig. S1. The equipment is designed with a heating plate set to maintain a temperature of 75 °C to facilitate ink drying and adhesion, an integrated ink reservoir, an ultrasonic disperser, and a high-precision nozzle. The optimized conditions for this study include a nozzle height of 35 mm, a step distance of 1 mm [33], and a flow rate ranging from 10 to 15 mL h^{-1} as a function of the material applied.

The fabricated multi-layered photoanodes include a $CaTiO_3$ electron collector bottom layer (1 mg cm^{-2}), an intermediate WO_3 conductive layer (0.75 mg cm^{-2}), and a $BiVO_4$ light-harvesting top layer (3 mg cm^{-2}), following the protocol established in previous studies [28]. These multi-layered photoanodes are subsequently decorated with Ni nanoparticles following two different approaches: i) by adding a Ni layer with varying loadings (0.5 and 1 mg cm^{-2}) as the top surface, and ii) by replacing the $BiVO_4$ top layer with a physical mixture of Ni (0.5 mg cm^{-2}) and $BiVO_4$ (3 mg cm^{-2}) as the final top layer. Table 1 summarizes the nomenclature used in this work for the different manufactured photoanodes.

Table 1
Sample coding for the different photoanode surfaces presented in this work.

Photoanode	Code	Top layer	Ni loading (mg cm^{-2})
$CaTiO_3/WO_3/BiVO_4$/Ni	CWBN0.5	Ni	0.5
$CaTiO_3/WO_3/BiVO_4$/Ni	CWBN1	Ni	1
$CaTiO_3/WO_3/BiVO_4$-Ni	CWBN-M0.5	Ni-$BiVO_4$ mixture	0.5
$CaTiO_3/WO_3/BiVO_4$	CWB	-	-
$CaTiO_3/BiVO_4$	CB	-	-

2.2. Characterization

2.2.1. Physicochemical and optical measurements

The crystallinity and chemical composition of the fresh and used photoanodes are assessed using powder X-ray diffraction (PXRD) measurements. The spectra are obtained using a PANalytical X'Pert PRO diffractometer equipped with Cu $K_{\alpha1}$ radiation ($\lambda = 1.5406$ Å) at room temperature. The instrument is operated at 40 kV and 40 mA and diffraction data are collected in a 2θ range of 5° to 70° with a step size of 0.02° using a continuous scan mode. A PIXcel detector is employed [30]. Scanning electron microscopy (SEM) is conducted with a JEOL JSM-7000 F field emission microscope, which features a Schottky-type electron gun, secondary electron (SE) detector, backscattered electron (BSE) detector, and Oxford's INCA X-sight Series Si(Li) penta-FET energy-dispersive X-ray spectroscopy (EDS) detector for spot, line, and mapping analysis. SEM images are acquired both on the surface and on the cross section of the fresh/used surfaces, at magnifications of 100X, 1kX, 5kX, and 20kX. Both secondary electron (SE) and backscattered electron (BSE) detectors are utilized for generating images, with additional elemental mapping performed using EDS for the bi-component photoanodes.

Diffuse reflectance spectroscopy (DRS) measurements are carried out over the 220–2200 nm wavelength range using a UV-Visible-NIR JASCO 770-V spectrometer, equipped with an integrating sphere coated with Spectralon and offering a spectral resolution of 1 nm. A Spectralon reference is used for 100 % reflectance measurements, while internal attenuators are employed to establish zero reflectance and minimize background noise. For DRS measurements, electrodes are directly placed in the holder, and powder samples are prepared as pellets. The measured reflectance spectra are subsequently converted to Kubelka-Munk (K-M) absorption factors to evaluate the absorption spectra of the samples. This conversion is performed using the K-M equation: $F(R) = (1\text{-}R_\infty)^2/(2\cdot R_\infty)$ ($R_\infty = R_{sample} / R_{standard}$, is the reflectance). The resulting UV-Vis-NIR absorption spectra obtained from the Kubelka-Munk equation for $CaTiO_3$ powder sample is fitted to Tauc formula, $(\alpha h\nu)^{1/n} = A(h\nu - E_g)$, where, α is the absorption coefficient, A is a constant, hν is photon energy, and n is a factor that depends on the bandgap electron transition: 0.5 for direct and 2 for indirect transitions. In the Kubelka-Munk approximation, F(R) is taken as proportional to the absorption coefficient (α), and is therefore used in place of α in the Tauc plot. Afterwards, the bandgap is obtained from the intersection of the linear fit with the abscissa axis in the $(\alpha h\nu)^{1/n}$ vs hν plot [34,35].

2.2.2. PEC characterization

PEC characterization is performed in a modified PEC filter-press reactor (Micro Flow Cell, ElectroCell A/s) adapted to be illuminated through a transparent methacrylate plate (PMMA, 92 % transparency) in the anodic compartment. The photoanode is exposed to visible LED lights (peak intensity at 450 nm) (Photolab LED 450–3, Apria Systems) with an intensity of 100 mW cm^{-2} (1 sun) under back illumination [28]. The dark cathode consists of a platinized titanium plate (ElectroCell). A 0.5 M $KHCO_3$ aqueous solution (ACS reagent, Thermo Scientific) is used as the electrolyte in both compartments, with a flow rate of 0.57 mL min^{-1} cm^{-2} and a pH of 8.7 to prevent $BiVO_4$ degradation [36]. The cell compartments are separated by a Nafion 117 ion exchange membrane (0.180 mm thick, > 0.9 meq·g^{-1} exchange capacity, Ion Power). A thin, leak-free Ag/AgCl electrode (3.4 M KCl) serves as the reference electrode.

On-off chronopotentiometry (*CP*) measurements are conducted using a potentiostat-galvanostat (AutoLab PGSTAT 302 N, Metrohm Hispania) for 30 min at a constant current density of 100 mA cm^{-2}. On-off linear sweep voltammetry (*LSV*) analyses are performed between −1.8 and −1 V (vs. Ag/AgCl), at a scan rate of 50 mV s^{-1}. Subsequently, the potential range is extended from −2 to 5 V (vs. RHE), maintaining the same scan rate, in order to evaluate the onset potential and the performance of the photoanodes during the OER. The measured potentials vs. Ag/AgCl electrode are converted to the reversible hydrogen electrode (RHE) scale according to the Nernst formula: $E_{RHE} = E_{Ag/AgCl} + 0.0591 \times pH + 0.197$. Electrochemical impedance spectroscopy (*EIS*) measurements are also conducted at a fixed voltage of −0.8 V vs. Ag/AgCl, with frequencies ranging from 10 kHz to 0.01 Hz, in order to assess the electron transfer resistance of the different photoanodes tested.

2.2.3. PEC performance

The photoanodes are tested in a divided filter-press reactor (Micro Flow Cell, ElectroCell A/s) operating under single-pass operation. O_2 production is evaluated at a constant current density of 100 mA cm^{-2} during continuous operation, with a platinized titanium plate serving as the dark cathode. An on-line gas chromatograph (990 Micro GC, Agilent), equipped with a Molsieve column, is utilized to quantify the concentrations of O_2 and H_2 produced at the photoanode and cathode outlets, respectively. All (photo)electrochemical tests are conducted in triplicate using freshly prepared photoanodes to ensure the reproducibility of the samples. For O_2 and H_2 production measurements, samples were collected every 5 min to monitor product evolution.

The PEC performance of the electrolyzer is evaluated in terms of:

- Production rate, $r\left(\frac{\mu mol}{cm^2 h}\right)$: the amount of O_2 and H_2 produced per photoanode and cathode geometric area, respectively, during the experimental time.

$$r = \frac{N_F}{A} \tag{1}$$

where N_F is described as the molar flux of the products (μmol h^{-1}) and A is the geometric area of the electrodes (10 cm^2).

- Applied Bias Photon-to-Current Efficiency, *ABPE* (%): this represents the efficiency of converting solar energy into chemical energy at the photoanode, considering the applied bias.

$$ABPE(\%) = J_{ph}\frac{1.23 - V_{app}}{P_{light}}\cdot 100\% \tag{2}$$

where J_{ph} represents the photocurrent density (mA cm^{-2}), V_{app} represents the applied bias versus RHE (V), and P_{light} is the total applied light intensity of AM 1.5 G (100 mW cm^{-2}).

- Faradaic Efficiency, *FE* (%): selectivity of the external current density applied toward the formation of H_2 at the cathode.

$$FE(\%) = \frac{z \quad F \quad N_F}{Q}\cdot 100\% \tag{3}$$

where *z* is the number of electrons exchanged, which in the case of H_2 is 2, *F* represents the Faraday constant (96485 C mol^{-1}), N_F reflects the molar flux of H_2, and Q is the total current density applied (A).

- Cathodic Energy Efficiency, *CEE* (%): the amount of energy used in the formation of H_2 at the cathode.

$$CEE(\%) = FE\cdot\frac{E_T}{V_{app}} \tag{4}$$

where *FE* represents the faradaic efficiency and E_T is the theoretical potential for hydrogen production (V).

3. Results and discussion

3.1. Physicochemical and optical measurements

PXRD analyses of prepared photoanodes (Fig. 1) reveal the presence of perovskite $CaTiO_3$ (ICDD PDF No. 01–086–1393), monoclinic WO_3 (ICDD PDF No. 01–071–2141), monoclinic $BiVO_4$ (ICDD PDF No.00–014–0688), and metallic Ni (ICDD PDF No. 00–004–0850)

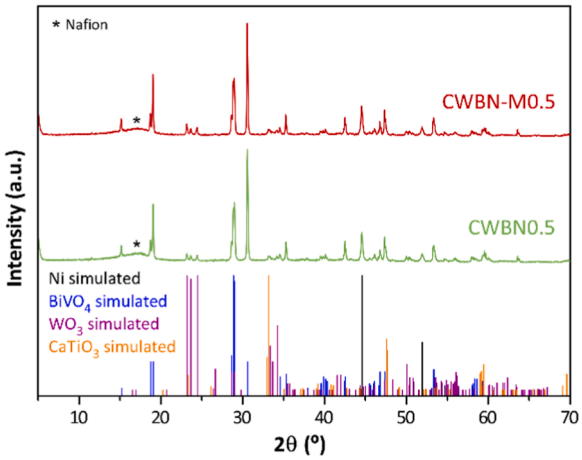

Fig. 1. PXRD patterns of prepared CWBN0.5 and CWBN-M0.5 photoanodes. For comparative purposes, the simulated patterns of the identified $CaTiO_3$ (in orange), WO_3 (in purple), $BiVO_4$ (in blue), and Ni (in black) structures have been included.

structures. The identification is made based on the data retrieved from the Powder Diffraction File (PDF) database [37]. This confirms the maintenance of all structures during the photoanode preparation process and aligns with the mass content of each layer, with $BiVO_4$ reflections being the most intense contributions due to its higher mass content. The broad, low-intensity hump observed at $2\theta = 15–17°$ on the photoelectrodes (marked with an asterisk) results from the Nafion binder (a sulfonated tetrafluoroethylene-based fluoropolymer-copolymer) of poor crystallinity.

SEM images of the photoelectrode surfaces and cross sections are captured at various magnifications using secondary electron (SE) and backscattered electron (BSE) detectors for image generation, and EDS for elemental mapping of the multicomponent surfaces, as previously mentioned, to assess the large-scale homogeneity and fine details of the microstructure. Fig. 2a and Fig. 3a show SE images at 1 kX of fresh surfaces of the CWBN0.5 and CWBN-M0.5 photoanodes, together with the corresponding image built from the combination of BSE image and EDS mapping. The unused surface of CWBN0.5 appears mainly covered by Ni nanoparticles of 80–200 nm (depicted as green colored spots), while $BiVO_4$ micrometric crystallites (1–7 μm), observable as polydisperse purple-colored diffuse grains, remain beneath the outermost Ni/Nafion layer (please see Fig. S3 in the Supporting Information). On the contrary, in the mixed top layer structure (CWBN-M0.5), $BiVO_4$ crystallites emerge at the photoelectrode surface homogenously dispersed along a finer distribution of Ni particles (please see Fig. S4 in the Supporting Information).

For the analysis of the multi-layer stack structure, SEM analyses are also performed on the cross section of the photoelectrodes (Fig. 2b and Fig. 3b). The BSE images captured at 2.5 kX magnification reveal the layered structure developed during the multiple steps of the spray pyrolysis process, with a total thickness of approximately 15–30 μm. Each compound is observable as bright particles dispersed within the Nafion matrix (depicted as darker gray areas). Below, the FTO coating is appreciable as a bright, thin film that covers. Clearer evidence of the distribution of the components in each layer is obtained from the EDS mapping of the metal elements. FTO film (300 nm) is identified by the distribution of tin (pink colored). The absorber $CaTiO_3$ (orange colored) coating consists of 0.5–1 μm crystallites and exhibits a thickness ranging from 3 to 6 μm. Over it a thinner coating (1–3 μm light blue) comprised of WO_3 submicrometric crystallites (100–500 nm) is observed. At the top of the cross-section, a dispersion of Ni nanoparticles (green spots) and micrometric $BiVO_4$ crystallites (purple areas), beneath the Ni for

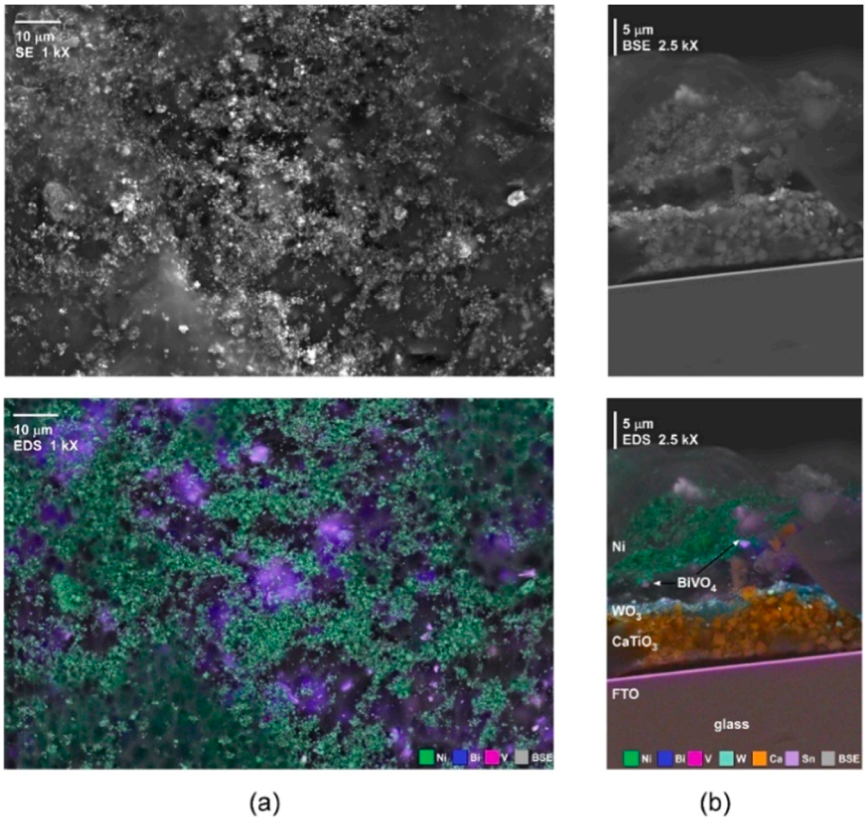

Fig. 2. SE (up) and EDS mapping (down) SEM images for CWBN0.5 fresh photoanode: (a) photoelectrode surface at 1 kX magnification and (b) photoelectrode cross section at 2.5 kX magnification.

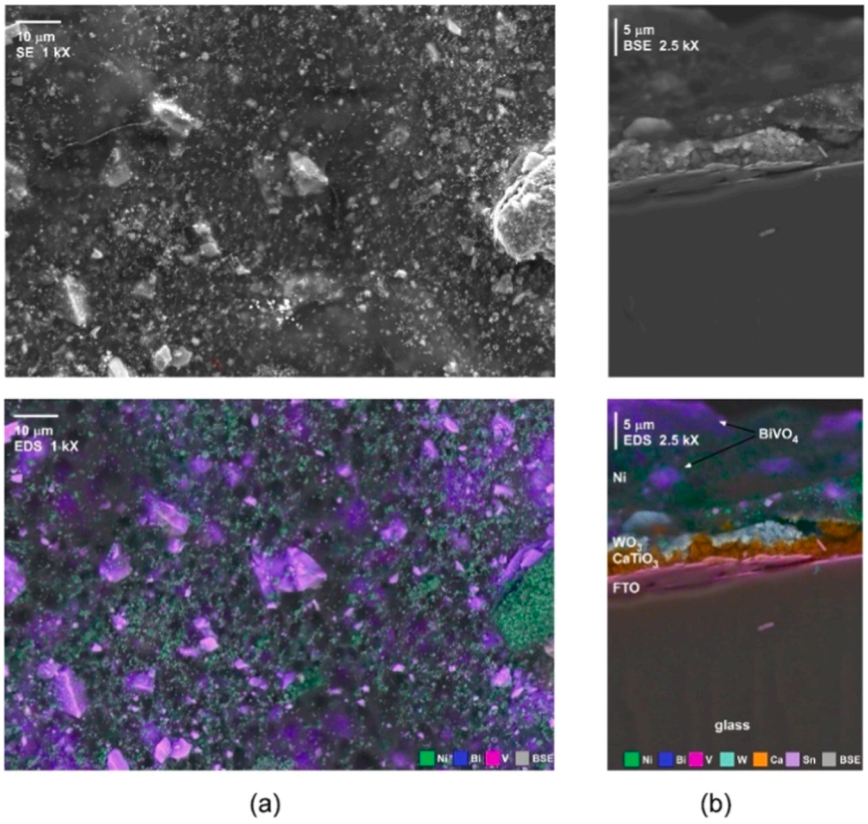

Fig. 3. SE (up) and EDS mapping (down) SEM images for CWBN-M0.5 fresh photoanode: (a) photoelectrode surface at 1 kX magnification and (b) photoelectrode cross section at 2.5 kX magnification.

CWBN0.5 (Fig. 2b-down) or all mixed together for CWBN-M0.5 (Fig. 3b-down), can be observed, with a thickness of approximately 15–20 µm.

UV-Vis-NIR DRS was performed on the back side of the photoelectrodes to analyze their optical properties prior to conducting light-driven experiments in a back-illumination configuration. Fig. 4 shows the absorption spectra after their transformation using the Kubelka-Munk (K-M) function. The spectra show the absorption edge for both prepared surfaces at *ca.* 350 nm, which fits rather well with the absorption spectra for the pristine $CaTiO_3$ presented for comparison (green dashed line). Since the $CaTiO_3$ bottom layer provides a homogeneous coating as demonstrated in a previous work [28], the underlying layers in back-illumination configuration are fully covered and the optical properties of the photoelectrode are almost coincident with $CaTiO_3$ single component one. Only small differences with respect to pristine powder are observed. These distortions in the spectra are caused by the FTO film of the glass support, measured for a pristine substrate before layer deposition (grey dashed line). The bandgap calculation using the Tauc method for $CaTiO_3$ powder is presented in the Supporting Information (Fig. S7 and Table S1). The absorption edge (3.55 eV) and the corresponding optical bandgap calculated for direct (3.63 eV) and indirect (3.48 eV) transitions are in agreement with the values reported by other authors [38]. It should be noted, however, that the Kubelka–Munk transformation assumes optically homogeneous and infinitely thick scattering media, which may not be fully applicable to multilayer photoelectrodes. As such, the apparent absorbance may not capture subtle contributions from underlying layers (WO_3 and $BiVO_4$, with absorption edges at 439 and 501 nm, respectively [22]; even if these influence the overall photoresponse under illumination.

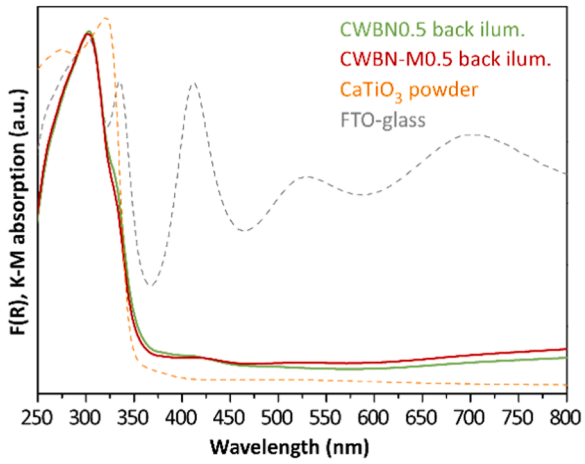

Fig. 4. UV-Vis-NIR absorption spectra derived from Kubelka-Munk function for prepared photoanodes in back-illumination configuration. $CaTiO_3$ powder and FTO substrate spectra (dashed lines) are shown for comparison purposes.

3.2. PEC characterization and performance

Fig. 5 presents the results of the PEC response for different photoanode configurations, including CP (Figs. 5a, 5d), EIS (Figs. 5b, 5e), and LSV (Figs. 5c, 5f) measurements.

Fig. 5a shows that the multi-layered photoanodes minimize the required external potential compared to the bi-layered CB surface, which is crucial to improve the overall energy efficiency of the PEC system, demonstrating the potential of the prepared photoanodes for more efficient solar energy conversion. These findings also indicate that the multi-layered structure is more effective in reducing the energy loss during the PEC process, which can be linked to better light harvesting, charges separation, and electrons transfer to the cathode. A schematic representation of the proposed charge transport mechanisms in the

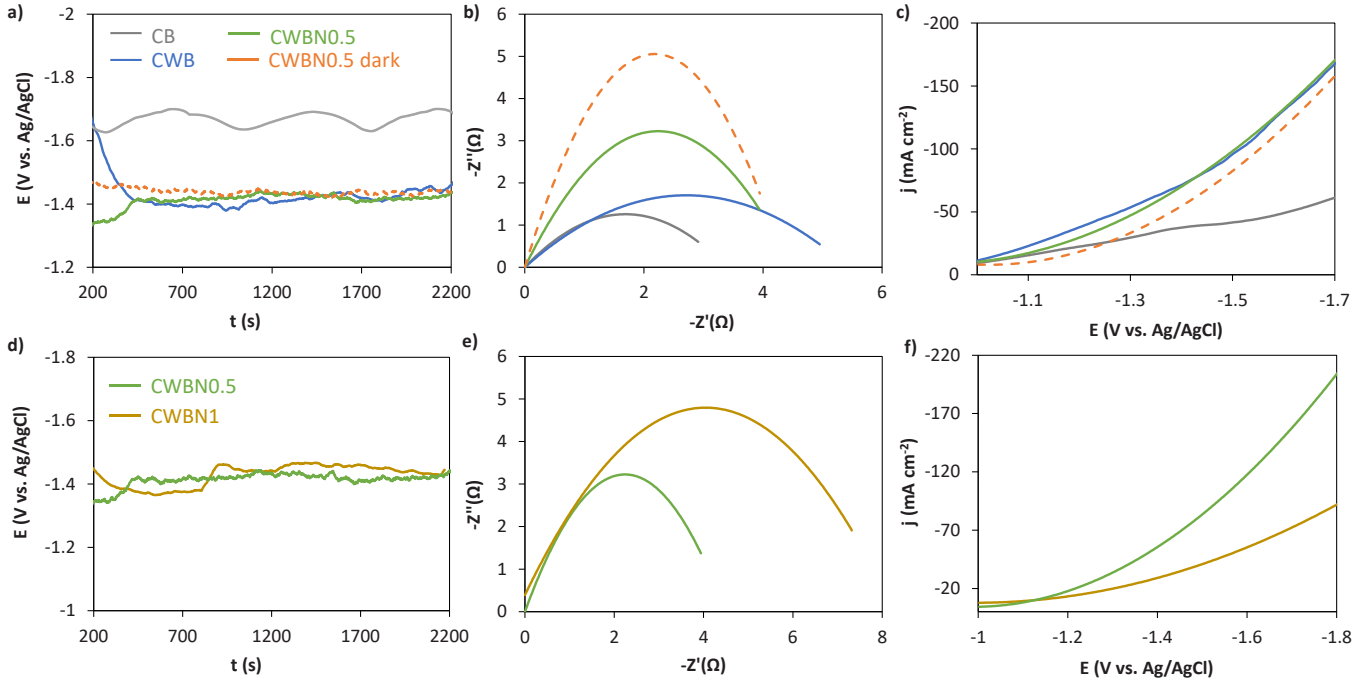

Fig. 5. a) CP curves, b) EIS Nyquist plots, and c) LSV curves for CB, CWB and CWBN0.5. d) CP curves, e) EIS Nyquist plots, and f) LSV curves as a function of Ni loading for CWBN0.5 and CWBN1 layer-by-layer photoanodes.

multilayer photoanodes is displayed in the Supporting Information (Fig. S2). This diagram highlights the enhanced separation and transfer of electrons and holes resulting from both the bandgaps and the favourable positions of the conduction and valence bands CB and VB, respectively. Specifically, $CaTiO_3$ exhibits a CB edge at approximately −0.94 V vs. NHE and a VB at +2.15 V vs. NHE [39]. These energy levels enable photogenerated electrons to migrate first toward WO_3 (CB ≈ +0.50 V) and subsequently to $BiVO_4$ (CB ≈ −0.39 V), while the corresponding holes transfer to the VB levels of WO_3 (≈ +3.30 V) and $BiVO_4$ (≈ +2.04 V), where they effectively drive the oxygen evolution reaction [40,41].

Furthermore, Fig. 5b shows a smaller Nyquist plot radius for CWBN0.5 compared to the behaviour of CWB, suggesting an enhanced electron transfer process, which aligns with previous findings [28], and suggests that the illumination promotes a more efficient electron-hole separation. By contrast, the addition of an extra Ni layer (4 layers in total) results in increased resistance in comparison with the CB photoanode (2 layers), as evidenced by the larger radius of the semicircle in the EIS results for CWBN0.5. This observation is consistent with SEM images (Fig. 2b), which show that the addition of Ni increases the film thickness and causes significant agglomeration of the particles, that can create charge transport barriers, thereby reducing the charge transfer efficiency and the overall photoanode performance as previously reported [42]. However, Ni incorporation may enhance the stability of the photoanodes, as Ni coatings can protect the underlying photoelectrode material from degradation, thus extending its operational lifetime under real electrolysis conditions [43]. Similarly, protective surface modifications such as NiFeOx/Tb(OH)x have also been demonstrated to stabilize $BiVO_4$ under prolonged operation [44].

LSV tests (Fig. 5c) confirm that the CWB and CWBN0.5 photoanodes exhibit similar PEC performance within the evaluated applied voltage, where the optimal potential window is located between −1.3 and −1.7 V vs. Ag/AgCl. In particular, for CWBN0.5, Fig. 5c shows that the photocurrent density increases upon illumination (green trace) compared to the dark conditions (orange dashed trace), thereby confirming the beneficial effect of light on PEC performance.

Moreover, regarding the effect of the catalytic Ni loading on PEC performance under illumination (Fig. 5d), the CWBN1 photoanode exhibits a less stable response. This behavior may be attributed to catalyst saturation caused by particle agglomeration, which hinders mass transfer and limits accessibility to the active sites [43]. Therefore, moderate Ni loading may enhance catalyst activity by promoting its transformation into more active species, thereby reducing the photoanode overpotential [45,46]. Moreover, literature shows that electron transfer is facilitated at lower charges because the layers are closer to the interface of the substrate [47]. EIS spectra displayed in Fig. 5e further support these observations, showing that CWBN1 photoelectrodes present a larger Nyquist-plot radius, which corresponds to a higher charge transfer resistance. Besides, lower Ni loadings (0.5 mg cm^{-2}) in the photoanode lead to higher current densities at the cathode under a wide potential window, as displayed in Fig. 5f.

Overall, this Ni catalyst loading is selected as the optimal in the present work (CWBN0.5), leading to a slightly less negative required cathodic voltage (–1.41 V vs. Ag/AgCl) compared to results achieved in the dark (–1.44 V vs. Ag/AgCl), resulting in a light-induced potential shift of 0.03 V, which is consistent with previous results [48].

Moreover, Fig. 6 displays the PEC characterization and performance results for the CWBN-M0.5 photoanode configuration, compared with the CWBN0.5 photoanode.

The CP results shown in Fig. 6a clearly reveal a lower external cathodic potential required for CWBN-M0.5 (–1.17 V vs. Ag/AgCl) compared to CWBN0.5 (–1.41 V vs. Ag/AgCl). This Ni-$BiVO_4$ physical mixture in the top layer also leads to reduced charge recombination, as evidenced by the lower impedance and resistance results (Fig. 6b). The fitted parameters are presented in the Supporting Information (Table S4), and the equivalent circuit used to provide further insight into the interfacial charge transfer is shown in Fig. S8. The obtained charge transfer resistance (R_{ct}) of 15.1 Ω indicates enhanced charge transfer, exhibiting slightly lower resistance values than those typically reported for WO_3/$BiVO_4$-based photoanodes under similar PEC water splitting conditions [49,50]. The LSV tests presented in Fig. 6c further corroborate these findings, demonstrating a notable improvement in PEC performance, and suggesting that combining $BiVO_4$ and Ni into a single top layer may enhance both light harvesting and catalytic performance.

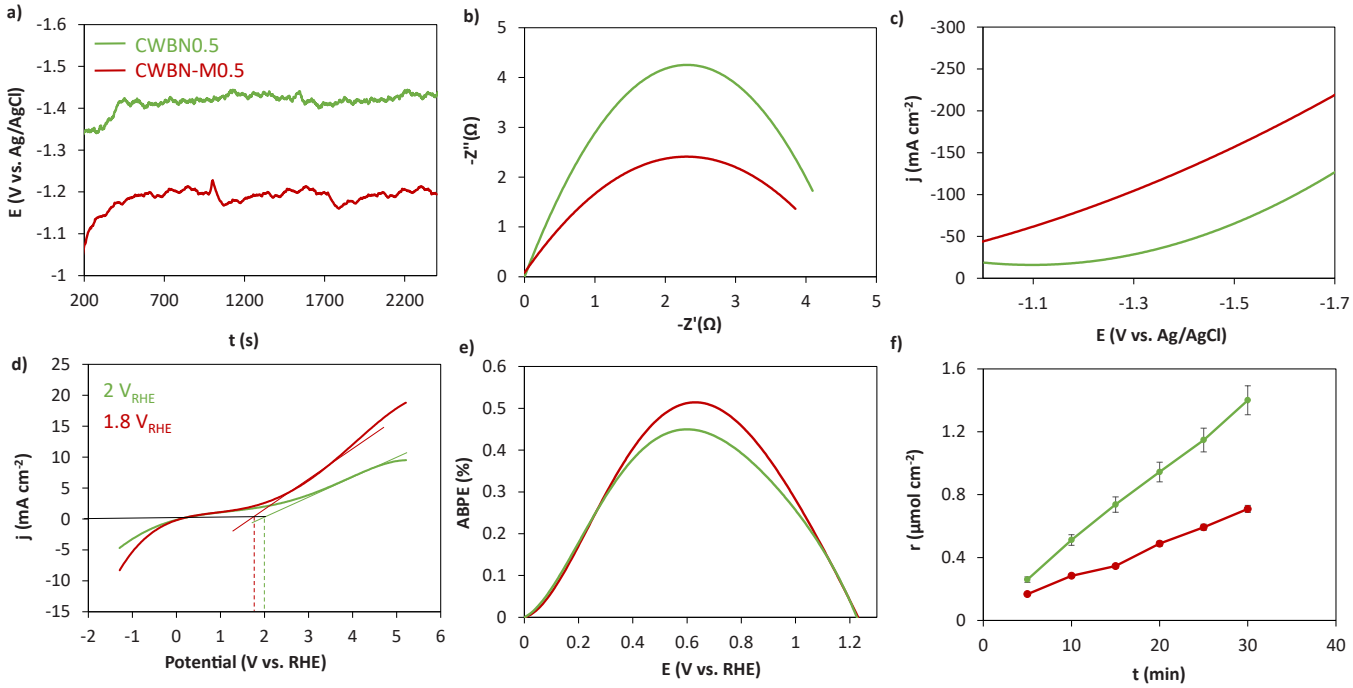

Fig. 6. a) CP, b) LSV, c) EIS, d) Onset potential, e) ABPE, f) Cumulative oxygen production rate for CWBN-M0.5 and CWBN0.5 under illumination.

Trotochaud et al. [47] studied Ni-Fe oxyhydroxide-based photoanodes and highlighted the role of the composition and layer thickness on catalytic activity, where a reduction in interfacial thickness may enhance accessibility to the active sites, promote a better interaction between the two components, and thus facilitate more efficient charge transfer. This trend is also in agreement with the SEM/EDS images shown above (Fig. 2 and Fig. 3.), which reveal a small decrease in the thickness of the top layer in the CWBN-M0.5 photoanodes, suggesting a closer contact between $BiVO_4$ and Ni. Such an interface promotes efficient hole transfer from $BiVO_4$ to Ni, favours the formation of surface hydroxyl species, and facilitates the activation of Ni into catalytically active Ni^{3+}/Ni^{4+} states, ultimately improving OER performance [51,52]. Besides this, Chen et al. [32] demonstrated that the incorporation of Ni into the $BiVO_4$ lattice leads to a reduction in particle size and promotes the formation of V^{4+} species and oxygen vacancies. These modifications facilitate faster charge carrier transport by minimizing the distance between generation and reaction sites, thereby enhancing optical absorption and overall PEC performance. This may explain the reduced Nyquist plot radius for CWBN-M0.5 compared to CWBN0.5, which is directly associated with enhanced charge transfer efficiency. Moreover, the SEM/EDS results presented above reveal $BiVO_4$ crystallites homogenously dispersed, together with a finer and uniform distribution of Ni particles in the CWBN-M0.5 photoanode. These observations, consistent with literature reports, suggest that the physical mixing of Ni with other elements can promote the formation of hybrid materials with enhanced PEC performance toward the OER [47]. Additionally, Fig. 6d shows that CWBN-M0.5 exhibits a higher attainable current density at the same potential level with a lower oxidation potential (1.8 V_{RHE}) compared to the independent layer-by-layer CWBN0.5 photoelectrode (2 V_{RHE}). This indicates a lower kinetic barrier which can improve overall PEC performance. In this regard, the CWBN-M0.5 photoanode reaches a maximized ABPE value of 0.52 % at 0.65 V vs. RHE, higher than that for the CWBN0.5 photoanode (0.45 %) as shown in Fig. 6e. Additional performance results of the HER (FE and CEE) can be seen in the Supporting Information (please see Table S2).

Fig. 6f depicts the O_2 evolution results for the studied photoanodes. The layer-by-layer CWBN0.5 photoelectrode exhibits significantly higher O_2 production, suggesting more effective OER catalysis due to a greater number of Ni active sites. Nevertheless, CWBN-M0.5 remains the most efficient photoanode configuration, given its markedly reduced external energy demand at practically relevant current densities. Similar to the findings reported by Gong et al. [53,54] and Zhu et al. [53,54], where an ultra-thin Ni film was employed as a protective and catalytic layer in silicon-based photoanodes, the controlled and homogeneous deposition of Ni can enhance the accessibility of active sites and improve charge transfer at the photoanode surface, ultimately boosting the efficiency of the OER process. In their work, a 2 nm Ni film contributed significantly to enhancing the photoanode performance by facilitating more efficient OER pathways, resulting in higher O_2 evolution compared to Ni-free configurations [55]. In our case, the incorporation of Ni into the $BiVO_4$ structure (Ni-$BiVO_4$) likely promotes similar effects, as the Ni sites may act as active centers for water oxidation while also improving the interfacial conductivity and suppressing charge recombination. Interestingly, despite the differences in O_2 production observed among the different photoanode configurations, the H_2 generation rate at the cathode remains relatively stable (23–24 µmol cm^{-2} h^{-1}), which is consistent with the constant current density applied during the measurements.

Fig. 7 presents the PXRD patterns of the photoanodes before and after PEC testing, revealing no significant shifts or degradation in the crystalline phases. The reflections corresponding to all constituent compounds remain unchanged, confirming the chemical and structural stability of the photoactive catalytic surfaces throughout PEC operation. Thus, the absence of phase changes in the PXRD patterns demonstrates exceptional stability of the prepared photoanodes, even after extended OER operation, which represents a crucial requirement for scalable PEC systems.

Complementary evidence of the CWBN-M0.5 and CWBN0.5 stability is provided with SEM-EDS analyses (Fig. 8 and Fig. S5-S6), which reveal no discernible morphological degradation or major compositional changes after PEC operation during the light-driven OER. The pre- and post-test SEM images exhibit consistent surface morphology, where the outermost surface remains comprised by a dispersion of Ni nanoparticles and $BiVO_4$ crystallites, despite slight material leaching being appreciable compared to the fresh photoelectrodes. Critically, no signs of severe corrosion, particle agglomeration, or delamination are observed.

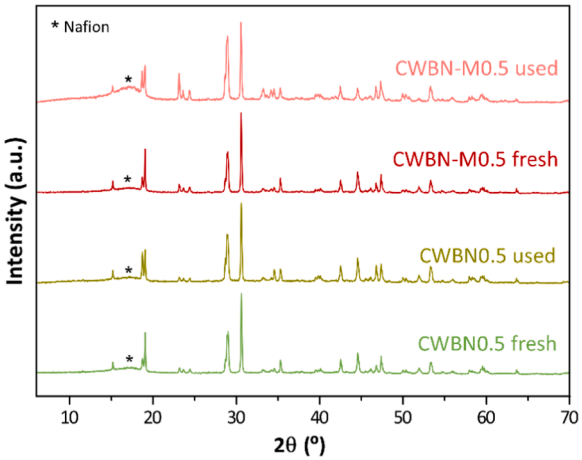

Fig. 7. PXRD patterns of CBWN0.5 and CWBN-M0.5 photoanodes before (fresh) and after (used) the PEC reaction.

EDS elemental mapping further corroborates this structural resilience, confirming the retention of the original composition. These findings align with the PXRD results (Fig. 7), collectively demonstrating that the photoanodes maintain both structural and chemical integrity after operation under relevant current densities, thereby helping to prevent the efficiency degradation typically observed in photoelectrode systems over time. This robustness is particularly noteworthy for solar-driven applications, where consistent performance under continuous light exposure is essential.

In addition to the characterization analyses, the stability of the PEC system has been evaluated at longer operational times using the optimized photoanode. Fig. 9 shows the evolution of the required cathodic potential at -100 mA cm^{-2} when using CWBN-M0.5 during 8 h of continuous operation under visible light.

Throughout the entire experiment, the system maintained an almost constant required potential, demonstrating pseudo-stable PEC performance under prolonged high-current conditions. This behaviour is particularly relevant for approaching real PEC scenarios and for future integration of these photoanodes in CO_2 electroreduction systems, where long-term operation at high current densities is essential for practical applications.

Finally, a comparative overview of the PEC performance metrics reported for $WO_3/BiVO_4$-based photoanodes employed in solar water splitting applications (with standard Pt cathodes) is carried out. It should be noted that, while the cathode material remains consistent across studies, direct comparison of photoanode performance (e.g., photocurrent density, ABPE, O_2 evolution rate, etc.) is inherently complex due to substantial variations in deposition methods, material composition, photoelectrode architecture, photoreactor design, electrolyte nature, and operation conditions, which hinder straightforward assessment of PEC performance. Although the O_2 evolution rates obtained with CWBN-M0.5 and CWBN0.5 are lower than those reported in the literature (please see Table S3 in the Supporting Information), it is important to note that most comparative studies are conducted under low fixed anodic potentials. In contrast, the photoanode configuration developed in this work operates at high and constant cathodic current densities. This setup provides a more realistic scenario for practical PEC systems and facilitates future integration with CO_2 reduction processes [53]. Importantly, operating under fixed current conditions at the cathode may result in partial energy diversion from the OER, potentially contributing to the lower O_2 evolution rates observed. Zhang et al. [12] have noted that high current densities can adversely affect the electrocatalyst activity and stability due to factors such as phase transitions,

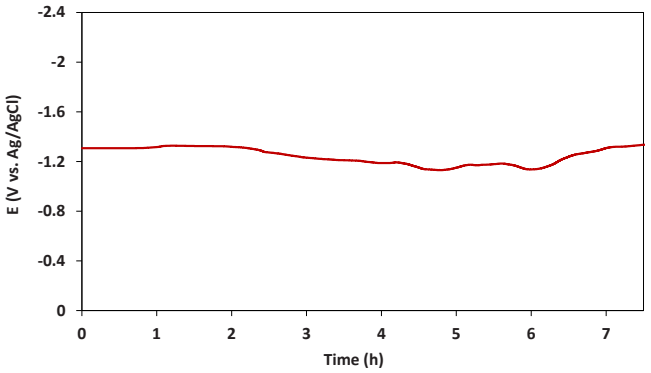

Fig. 9. Chronopotentiometry measurement of CWBN-M0.5 at -100 mA cm^{-2} during 8 h of continuous operation under visible light.

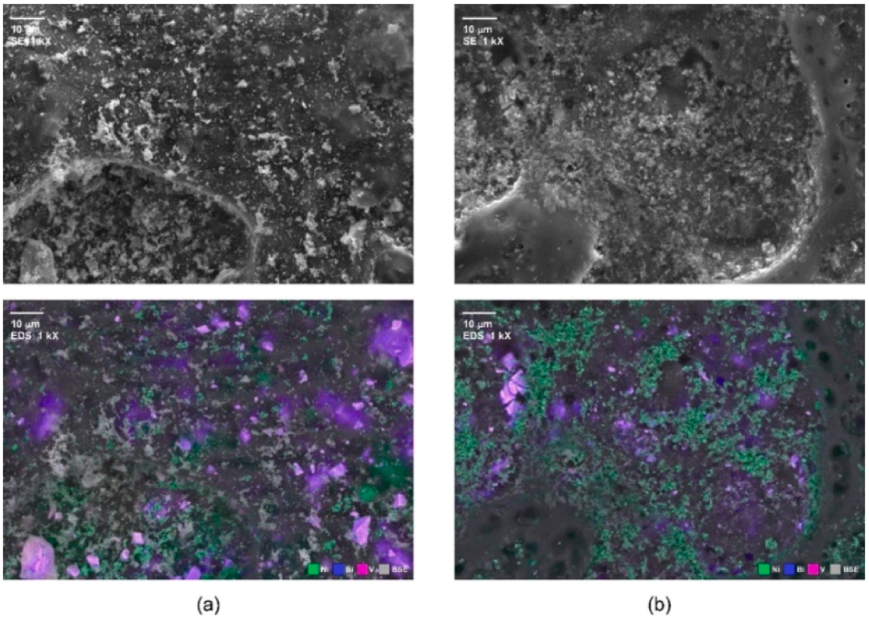

Fig. 8. SEM (up) and EDS mapping (down) images at 1 kX magnifications for (a) CWBN0.5 and (b) CWBN-M0.5 photoanode surfaces after the PEC reaction.

bubble dynamics, and limited mechanistic understanding at the electrochemical interface under such conditions. Despite these challenges, the photoelectrode architectures investigated in this study exhibit remarkable structural stability under relevant current densities, with no observable degradation or phase change after prolonged use, thus preventing the typical degradation of photoelectrodes over time at high current densities. This robustness under demanding conditions underscores their potential for implementation in integrated PEC systems, where operational stability represents a critical factor.

These results demonstrate their potential for integration into PEC systems for solar-driven CO_2 conversion or water splitting, which could significantly reduce external energy input requirements. Altogether, these findings advance the development of efficient and durable PEC pathways for sustainable energy applications.

4. Conclusions

This study demonstrates the potential of multi-layered Ni-decorated $CaTiO_3/WO_3/BiVO_4$ photoanodes for efficient solar-driven water oxidation in photoelectrochemical systems. By integrating photoactive materials with optimized architecture and surface decoration, the proposed photoanodes enable stable operation at technologically relevant current densities while minimizing the external energy input required.

Comparing the performance of layer-by-layer photoanodes with different Ni contents, excessive Ni loading (1 mg cm^{-2}) led to decreased performance, likely due to increased charge transfer resistance and light-blocking effects associated with greater photoanode thickness. By contrast, a Ni loading of 0.5 mg cm^{-2} provided a balanced enhancement of catalytic activity and light harvesting, highlighting the importance of precise interfacial engineering in multi-layer photoanodes design.

Among the tested configurations, the CWBN-M0.5 photoanode, consisting of a mixed Ni-$BiVO_4$ top layer, exhibited the best performance, achieving a cathodic voltage of −1.17 V vs. Ag/AgCl at −100 mA cm^{-2} with visible-light illumination. This clearly outperformed the traditional layer-by-layer structure, representing a 20.5 % reduction in the required voltage (-1.41 V vs. Ag/AgCl), thereby enhancing the energy efficiency of the process. This resulted in a maximized applied bias photon-to-current efficiency (ABPE) of 0.52 %, with an O_2 production rate of 2 μmol cm^{-2} h^{-1}.

Overall, these findings underscore the significant potential of rationally engineered multi-layered photoelectrodes for efficient PEC applications. The demonstrated performance at high current densities supports the feasibility of such architectures in scalable solar fuel technologies and sets also the framework for future integration with photo-assisted CO_2 reduction systems.

Moreover, the photoanodes demonstrated structural and electrochemical stability under prolonged operation at relevant current densities, reinforcing their potential applicability in durable PEC systems.

CRediT authorship contribution statement

Sara Crespo: Investigation, Data curation. **Ivan Merino-Garcia**: Investigation, Validation, Data curation. **Maite Perfecto-Irigaray**: Investigation, Data curation. **Garikoitz Beobide**: Investigation, Data curation. **Jonathan Albo**: Validation, Conceptualization, Resources.

Declaration of Competing Interest

The authors declare that they have no known competing financial interests or personal relationships that could have appeared to influence the work reported in this paper.

Acknowledgements

The authors gratefully acknowledge the Grant PID2022–138491OB-C31 and PID2022–138968NB-C22 funded by MICIU/AEI/10.13039/501100011033 and by "ERDF/EU", the Grant TED2021–129810B-C21 and TED2021–129810B-C22 funded by MICIU/AEI/10.13039/501100011033/ and by the "European Union NextGenerationEU/PRTR" and the grant IT1722–22 funded by Eusko Jaurlaritza/Gobierno Vasco. I. Merino-Garcia also acknowledges Grant RYC2023–043378-I funded by MICIU/AEI/10.13039/501100011033 and by ESF+ ; and M. Perfecto-Irigaray gratefully acknowledges financial support from the Basque Government Education Department, Postdoctoral Researcher Program (POS-E_2023_1_0001).

Appendix A. Supporting information

Supplementary data associated with this article can be found in the online version at doi:10.1016/j.jece.2025.118854.

Data availability

No data was used for the research described in the article.

References

[1] International Energy Agency, Global Hydrogen Review 2023, Paris, Francia, 2023.
[2] G. Leonzio, A. Hankin, N. Shah, CO_2 electrochemical reduction: a state-of-the-art review with economic and environmental analyses, Chem. Eng. Res. Des. 208 (2024) 934–955, https://doi.org/10.1016/j.cherd.2024.07.014.
[3] Q. Dong, B. Wen, X. Zhao, P. Wang, X. Lyu, Electronic structure tailoring of $CuCo_2O_4$ for boosting oxygen evolution reaction, Sep Purif. Technol. 353 (2025), https://doi.org/10.1016/j.seppur.2024.128552.
[4] J. Li, Y. Ma, X. Mu, X. Wang, Y. Li, H. Ma, Z. Guo, Recent advances and perspectives on coupled water electrolysis for Energy-Saving hydrogen production, Adv. Sci. (2025), https://doi.org/10.1002/ADVS.202411964.
[5] K. Fernández-Caso, A. Peña-Rodríguez, J. Solla-Gullón, V. Montiel, G. Díaz-Sainz, M. Alvarez-Guerra, A. Irabien, Continuous carbon dioxide electroreduction to formate coupled with the single-pass glycerol oxidation to high value-added products, J. CO_2 Util. 70 (2023), https://doi.org/10.1016/j.jcou.2023.102431.
[6] K. Maeda, M. Higashi, B. Siritanaratkul, R. Abe, K. Domen, J. Am. Chem. Soc. 133 (2011) 12334–12337, https://doi.org/10.1021/ja203391w.
[7] A. Saravanan, P. Senthil Kumar, K.S. Khoo, P.L. Show, C. Femina Carolin, C. Fetcia Jackulin, S. Jeevanantham, S. Karishma, K.Y. Show, D.J. Lee, J.S. Chang, Biohydrogen from organic wastes as a clean and environment-friendly energy source: production pathways, feedstock types, and future prospects, Bioresour. Technol. 342 (2021), https://doi.org/10.1016/j.biortech.2021.126021.
[8] F.Y. Chen, Z.Y. Wu, Z. Adler, H. Wang, Stability challenges of electrocatalytic oxygen evolution reaction: from mechanistic understanding to reactor design, Joule 5 (2021) 1704–1731, https://doi.org/10.1016/j.joule.2021.05.005.
[9] R.-T. Gao, Z. Gao, N.T. Nguyen, J. Chen, X. Liu, L. Wang, L. Wu, Photoelectrochemical production of disinfectants from seawater, Nat. Sustain 8 (2025) 672–681, https://doi.org/10.1038/s41893-025-01530-y.
[10] H. Chen, R.T. Gao, K. Su, Z. Li, L. Wu, L. Wang, Re and ru Co-Doped transition metal alloy as a bifunctional catalyst for electrooxidation of glycerol to formate coupled with H_2 production, Angew. Chem. Int. Ed. 64 (2025), https://doi.org/10.1002/anie.202501766.
[11] R.P. Yan, X. Zou, Y. Liang, Y. Liu, F. Hu, Y. Mi, Electron and surface engineering of Ni_2P/MnP_4 heterojunction as high performance bifunctional electrocatalyst for amperage-level overall water splitting, J. Colloid Interface Sci. 669 (2024) 349–357, https://doi.org/10.1016/j.jcis.2024.05.002.
[12] X. Zhang, M. Jin, F. Jia, J. Huang, A. Amini, S. Song, H. Yi, C. Cheng, Noble-Metal-Free oxygen evolution reaction electrocatalysts working at high current densities over 1000 ma cm^{-2}: from fundamental understanding to design principles, Energy Environ. Mater. 6 (2023), https://doi.org/10.1002/eem2.12457.
[13] W. Wu, Z. Yan, L. Wang, X. Zhu, Y. Zhu, G. Liao, L. Zhu, Efficient WO_3 nanoplate arrays photoanode modified by ZnO nanosheets for enhanced charge separation and transfer to promote photoelectrochemical performances, Adv. Electron Mater. 10 (2024), https://doi.org/10.1002/aelm.202300777.
[14] A. Waghmare, V. Sharma, P. Shinde, S. Shah, A. Punde, Y. Hase, B. Bade, V. Doiphode, S. Rahane, S. Ladhane, M. Prasad, S. Rondiya, S. Jadkar, MoO_3/γ-In_2Se_3 heterostructure photoanodes for enhanced photoelectrochemical water splitting, J. Mater. Sci. Mater. Electronics 34 (2023), https://doi.org/10.1007/s10854-023-10526-3.
[15] H.T. Htet, Y. Jung, Y. Kim, S. Lee, Enhanced photoelectrochemical water splitting using $NiMoO_4/BiVO_4$/Sn-Doped WO_3 double heterojunction photoanodes, ACS Appl. Mater. Interfaces 16 (2024) 52383–52392, https://doi.org/10.1021/acsami.4c11095.
[16] H. Yang, S. Li, S. Yu, X. Yu, H. Zhao, C. Wang, D. Ping, J.Y. Zheng, Strategies for enhancing the stability of WO_3 photoanodes for water splitting: a review, Chem. Eng. Sci. 302 (2025), https://doi.org/10.1016/j.ces.2024.120894.
[17] P. Dong, J. Pan, L. Zhang, X.L. Yang, M.H. Xie, J. Zhang, Regulation of electron delocalization between flower-like (Co, Ni)-MOF array and WO_3/W photoanode for effective photoelectrochemical water splitting, Appl. Catal. B 350 (2024), https://doi.org/10.1016/j.apcatb.2024.123925.

[18] S. McMichael, P. Fernández-Ibáñez, J.A. Byrne, A review of photoelectrocatalytic reactors for water and wastewater treatment, Water 13 (2021), https://doi.org/10.3390/w13091198.
[19] S. Wang, S. Feng, B. Liu, Z. Gong, T. Wang, J. Gong, An integrated n-Si/$BiVO_4$ photoelectrode with an interfacial bi-layer for unassisted solar water splitting, Chem. Sci. 14 (2023) 2192–2199, https://doi.org/10.1039/d2sc06651c.
[20] J.H. Kim, J.S. Lee, Elaborately modified $BiVO_4$ photoanodes for solar water splitting, Adv. Mater. 31 (2019), https://doi.org/10.1002/adma.201806938.
[21] C.A. Bignozzi, S. Caramori, V. Cristino, R. Argazzi, L. Meda, A. Tacca, Nanostructured photoelectrodes based on WO_3: applications to photooxidation of aqueous electrolytes, Chem. Soc. Rev. 42 (2013) 2228–2246, https://doi.org/10.1039/c2cs35373c.
[22] I. Merino-Garcia, S. Crespo, M. Perfecto-Irigaray, G. Beobide, A. Irabien, J. Albo, Tailoring multi-layered $BiVO_4$/WO_3 photoanodes for an efficient photoelectrochemical gas-phase solar water splitting, Catal. Today 432 (2024), https://doi.org/10.1016/j.cattod.2024.114581.
[23] Z. Wang, X. Huang, X. Wang, Recent progresses in the design of $BiVO_4$-based photocatalysts for efficient solar water splitting, Catal. Today 335 (2019) 31–38, https://doi.org/10.1016/j.cattod.2019.01.067.
[24] I. Grigioni, K.G. Stamplecoskie, E. Selli, P.V. Kamat, Dynamics of photogenerated charge carriers in WO_3/$BiVO_4$ heterojunction photoanodes, J. Phys. Chem. C. 119 (2015) 20792–20800, https://doi.org/10.1021/acs.jpcc.5b05128.
[25] X. Li, J. Yu, J. Jia, A. Wang, L. Zhao, T. Xiong, H. Liu, W. Zhou, Confined distribution of platinum clusters on MoO_2 hexagonal nanosheets with oxygen vacancies as a high-efficiency electrocatalyst for hydrogen evolution reaction, Nano Energy 62 (2019) 127–135, https://doi.org/10.1016/j.nanoen.2019.05.013.
[26] H. Dixit, S. Porwal, B. Boro, M. Paul, S. Ghosh, S. Mishra, T. Singh, A theoretical exploration of lead-free double perovskite La_2NiMnO_6 based solar cell via SCAPS-1D, Opt. Mater. 131 (2022), https://doi.org/10.1016/j.optmat.2022.112611.
[27] K.P. Kangeyan, H.Y. Hafeez, B. Neppolian, S.K. Lakhera, Operando construction of nickel-modifiedamorphous 2D $CaTiO_3$ nanosheets for enhanced photocatalytic hydrogen production, Surf. Interfaces 44 (2024), https://doi.org/10.1016/j.surfin.2023.103750.
[28] J.A. Abarca, I. Merino-Garcia, G. Díaz-Sainz, M. Perfecto-Irigaray, G. Beobide, A. Irabien, J. Albo, Fabrication and optimization of perovskite-based photoanodes for solar-driven CO_2 photoelectroreduction to formate, Catal. Today 429 (2024), https://doi.org/10.1016/j.cattod.2023.114505.
[29] D. Kong, J. Qi, D. Liu, X. Zhang, L. Pan, J. Zou, Ni-Doped $BiVO_4$ with V^{4+} species and oxygen vacancies for efficient photoelectrochemical water splitting, Trans. Tianjin Univ. 25 (2019) 340–347, https://doi.org/10.1007/s12209-019-00202-1.
[30] B. Guan, J. Yu, S. Guo, S. Yu, S. Han, Porous nickel doped titanium dioxide nanoparticles with improved visible light photocatalytic activity, Nanoscale Adv. 2 (2020) 1352–1357, https://doi.org/10.1039/c9na00760a.
[31] E.K. Andreou, I. Vamvasakis, G.S. Armatas, Fabrication of high-surface-area mesoporous frameworks of β-$Ni(OH)_2$-$CdIn_2S_4$ p-n nano-heterojunctions for improved visible light photocatalytic hydrogen production, Inorg. Chem. Front. 11 (2024) 5273–5285, https://doi.org/10.1039/d4qi01092b.
[32] M. Chen, X. Chang, C. Li, H. Wang, L. Jia, Ni-Doped $BiVO_4$ photoanode for efficient photoelectrochemical water splitting, J. Colloid Interface Sci. 640 (2023) 162–169, https://doi.org/10.1016/j.jcis.2023.02.096.
[33] J.A. Abarca, G. Díaz-Sainz, I. Merino-Garcia, G. Beobide, J. Albo, A. Irabien, Optimized manufacturing of gas diffusion electrodes for CO_2 electroreduction with automatic spray pyrolysis, J. Environ. Chem. Eng. 11 (2023), https://doi.org/10.1016/j.jece.2023.109724.
[34] P. Makuła, M. Pacia, W. Macyk, How to correctly determine the band gap energy of modified semiconductor photocatalysts based on UV-Vis spectra, J. Phys. Chem. Lett. 9 (2018) 6814–6817, https://doi.org/10.1021/acs.jpclett.8b02892.
[35] J. Tauc, R. Grigorovici, A. Vancu, J. TAUC, , 1966, Optical Properties and Electronic Structure of Ge Optical Properties and Electronic Structure of Amorphous Germanium.
[36] S. Zhang, I. Ahmet, S.H. Kim, O. Kasian, A.M. Mingers, P. Schnell, M. Kölbach, J. Lim, A. Fischer, K.J.J. Mayrhofer, S. Cherevko, B. Gault, R. Van De Krol, C. Scheu, Different photostability of $BiVO_4$ in near-pH-neutral electrolytes, ACS Appl. Energy Mater. 3 (2020) 9523–9527, https://doi.org/10.1021/acsaem.0c01904.
[37] S. Gates-Rector, T. Blanton, The powder diffraction file: a quality materials characterization database, Powder Diffr. 34 (2019) 352–360, https://doi.org/10.1017/S0885715619000812.
[38] K. Ueda, H. Yanagi, H. Hosono, H. Kawazoe, Study on electronic structure of $CaTiO_3$ by spectroscopic measurements and energy band calculations, J. Phys. Condens. Matter 11 (1999) 3535–3546, https://doi.org/10.1088/0953-8984/11/17/311.
[39] M. Passi, B. Pal, A review on $CaTiO_3$ photocatalyst: activity enhancement methods and photocatalytic applications, Powder Technol. 388 (2021) 274–304, https://doi.org/10.1016/j.powtec.2021.04.056.
[40] S.N.S. Nasir, N.A. Mohamed, M.A. Tukimon, M.F.M. Noh, N.A. Arzaee, M.A. M. Teridi, Direct extrapolation techniques on the energy band diagram of BiVO4 thin films, Phys. B Condens Matter 604 (2021), https://doi.org/10.1016/j.physb.2020.412719.
[41] R. Radha, A. Srinivasan, P. Manimuthu, S. Balakumar, Tailored sunlight driven nano-photocatalyst: bismuth iron tungstate ($BiFeWO_6$), J. Mater. Chem. C. Mater. 3 (2015) 10285–10292, https://doi.org/10.1039/c4tc02284j.
[42] H.S. Guo, W. Zhao, Q. Ge, N. Jiang, M. Liu, H. Cong, Photoelectrochemical water splitting improved by a cucurbit[7]uril-induced ternary heterojunction, Chem. Eng. J. 505 (2025), https://doi.org/10.1016/j.cej.2025.159340.
[43] Y.-C. Lin, J.-Y. Uan, N. Devi, A. Arpornwichanop, Y.-S. Chen, Development of calcined Ni/Fe layered double hydroxide for the anode electrode of an anion exchange membrane water electrolysis, n.d. ⟨https://ssrn.com/abstract=5082120⟩.
[44] Y. Chen, J. Huang, J. Zhou, X. Li, H. Yang, Y. Huang, Combinational effect of NiFeOx/Tb(OH)x as hole extractor for enhanced charges separation and stability of $BiVO_4$ photoanode for solar water splitting, Mater. Today Adv. 25 (2025), https://doi.org/10.1016/j.mtadv.2024.100554.
[45] L. Yang, H. Ren, Q. Liang, K.N. Dinh, R. Dangol, Q. Yan, Ultrathin amorphous nickel doped cobalt phosphates with highly ordered mesoporous structures as efficient electrocatalyst for oxygen evolution reaction, Small 16 (2020), https://doi.org/10.1002/smll.201906766.
[46] C. Tan, X. Cao, X.J. Wu, Q. He, J. Yang, X. Zhang, J. Chen, W. Zhao, S. Han, G. H. Nam, M. Sindoro, H. Zhang, Recent advances in ultrathin Two-Dimensional nanomaterials, Chem. Rev. 117 (2017) 6225–6331, https://doi.org/10.1021/acs.chemrev.6b00558.
[47] L. Trotochaud, S.L. Young, J.K. Ranney, S.W. Boettcher, Nickel-Iron oxyhydroxide oxygen-evolution electrocatalysts: the role of intentional and incidental iron incorporation, J. Am. Chem. Soc. 136 (2014) 6744–6753, https://doi.org/10.1021/ja502379c.
[48] X. Yun, Y. Lei, Z. Wang, X. Bo, Y. Ma, Highly enhanced photoelectrocatalytic activity of NiFe/Ni/$BiVO_4$ photoanode by a facile photoelectron-activation process in neutral solution, J. Photochem. Photobio. A Chem. 458 (2025), https://doi.org/10.1016/j.jphotochem.2024.115950.
[49] S. Liu, R.T. Gao, R. Zhang, Z. Wang, X. Liu, T. Nakajima, X. Zhang, Y. Su, L. Wang, Tungsten induced defects control on $BiVO_4$ photoanodes for enhanced solar water splitting performance and photocorrosion resistance, Appl. Catal. B 298 (2021), https://doi.org/10.1016/j.apcatb.2021.120610.
[50] J.E. Carrera-Crespo, I. Fuentes-Camargo, R.E. Palma-Goyes, U.M. García-Pérez, J. Vazquez-Arenas, I. Chairez, T. Poznyak, Unrevealing the effect of transparent fluorine-doped tin oxide (FTO) substrate and irradiance configuration to unmask the activity of FTO-$BiVO_4$ heterojunction, Mater. Sci. Semicond. Process 128 (2021), https://doi.org/10.1016/j.mssp.2021.105717.
[51] N. Hales, T.J. Schmidt, E. Fabbri, Reversible and irreversible transformations of Ni-based electrocatalysts during the oxygen evolution reaction, Curr. Opin. Electrochem 38 (2023), https://doi.org/10.1016/j.coelec.2023.101231.
[52] B. Wang, T. Fukushima, H. Minamimoto, A. Lyalin, K. Murakoshi, T. Taketsugu, Enhancing the oxygen evolution reaction by tuning the electrode–electrolyte interface in nickel-based electrocatalysts, Commun. Chem. 8 (2025), https://doi.org/10.1038/s42004-025-01508-z.
[53] M. Gong, Y. Li, H. Wang, Y. Liang, J.Z. Wu, J. Zhou, J. Wang, T. Regier, F. Wei, H. Dai, An advanced Ni-Fe layered double hydroxide electrocatalyst for water oxidation, J. Am. Chem. Soc. 135 (2013) 8452–8455, https://doi.org/10.1021/ja4027715.
[54] Y. Zhu, C. Cao, S. Tao, W. Chu, Z. Wu, Y. Li, Ultrathin nickel hydroxide and oxide nanosheets: synthesis, characterizations and excellent supercapacitor performances, Sci. Rep. 4 (2014), https://doi.org/10.1038/srep05787.
[55] Z.Q. Wang, H.J. Wang, Fabrication of cocatalyst NiO-Modified $BiVO_4$ composites for enhanced photoelectrochemical performances, Front. Chem. 10 (2022), https://doi.org/10.3389/fchem.2022.864143.